Design of memristor materials from ordered-vacancy zincblende semiconductors

Shao-Gang Xu,[1,2] Peng Zhang,[1,*] and Xiuwen Zhang[1,†]

[1]*Shenzhen Key Laboratory of Flexible Memory Materials and Devices, Key Laboratory of Optoelectronic Devices and Systems of Ministry of Education and Guangdong Province, College of Physics and Optoelectronic Engineering, Shenzhen University, Shenzhen 518060, People's Republic of China*

[2]*Department of Physics, Southern University of Science and Technology, Shenzhen 518055, People's Republic of China*

(Received 17 August 2020; accepted 19 January 2021; published 8 February 2021)

Memristors with promising applications in nonvolatile memory and unconventional computing have attracted much interest for both materials study and device development. Memristors are not commonly realized in zincblende-like semiconductors that could have optimum lattice matching with Si or GaAs substrates in semiconductor technologies, whereas often based on metal oxides with movable oxygen vacancies. Here, we propose the ordered-vacancy zincblende (OVZ) semiconductors as a type of memristor materials. Based on first-principles calculations on the Al_2-X-Y_4 group of semiconductors, we select Al_2CdS_4 as the best candidate that is lattice matched to Si, with medium energy barriers of ∼1 eV for vacancy/ion diffusion, comparable to the metal-oxide memristor materials, suggesting that Al_2CdS_4 could be segregated into ion-rich versus vacancy-rich structures via ion drift under electric operation. We find from defect calculations that both V_{Cd} and Cd_i are shallow defects, suggesting a bipolar conduction with electron transport dominated. We further find that the electron-rich Al_2CdS_4 structure can be both electrically conductive and optically transparent, showing potential applications as transparent memristors. Our study therefore opens the way of designing OVZ memristor materials with good compatibility with semiconductor technologies, as well as potentially optimum properties for memristor devices.

DOI: 10.1103/PhysRevMaterials.5.024603

I. INTRODUCTION

Since the prediction [1] and discovery [2] of the fourth passive circuit element, memristor, this type of electronic device and the related materials have drawn substantial attention, due to their promising applications in nonvolatile memory technologies and next-generation artificial intelligent computations. Many studies on memristor materials are focusing on metal oxides, such as ZnO [3–5], indium−gallium−zinc oxide [6], aluminum oxide [7], hafnium oxide [8], tantalum oxide [9], $BaTiO_3$ [10,11], $KNbO_3$ [12], NiO [13], TiO_2 [14], WO_3 [15], with the conducting filaments formed by their defective oxygen vacancies, whereas abundant vacancy defects could lower the materials' stability. However, in ordered-vacancy compounds [16–24], there are a significant amount of nondefective atomic vacancies formed in stable crystal structures. Such intrinsic vacancies could be mixed with the defective vacancies and offer fast drift conducting channels for them as well as the related defective interstitials, speeding up the formation of conducting channels under external electric field. Therefore, the ordered-vacancy compounds could offer better performance for memristor devices as compared to the vacancy-defective materials. Ordered-vacancy zincblende (OVZ) semiconductors [16] are a special class of ordered-vacancy materials that are less studied comparing to the vacancy-free diamondlike materials with significant applications in semiconductor technologies [25]. The mechanism for the formation of abundant vacancies and their ordering patterns was studied extensively [26–32]. The OVZ semiconductors could be naturally lattice-matched with their parent zincblende/diamondlike materials, while their abundant vacancies in the lattice could offer much better ion/vacancy conductivity than the latter. The flexibility of OVZ semiconductors such as variable distributions of vacancies could render them suitable candidates for the electronic devices that require both electronic and ionic transport like memristors [1,2,33].

In this paper, we studied the physical properties of both pristine and defective OVZ semiconductors as potential candidates for memristor materials. Focusing on the Al_2-X-Y_4 group of semiconductors, we select Al_2CdS_4 as the best candidate based on first-principles calculations of pristine materials. Al_2CdS_4 is stable in the tetragonal OVZ structure (space group No. 82) with a wide band gap of 3.87 eV from Heyd−Scuseria−Ernzerhof (HSE06) [34] and a small lattice mismatch (>0.35% and <2.5%) on Si(GaAs) substrates. Our defect calculations on Al_2CdS_4 show that at anion-rich condition and low-medium growth temperature, Al_2CdS_4 could be synthesized as a high-resistance semiconductor with rather low defect and carrier concentrations. We find from nudged elastic band (NEB) [35] calculations that the energy barriers for the diffusion of Cd vacancy/ion in Al_2CdS_4 between nearby available lattice sites are ∼1 eV, similar to the energy barriers found for the defect transport in metal-oxide memristor materials [4,36], indicating that Al_2CdS_4 could be segregated into ion-rich versus vacancy-rich regions via ion

*pengzhang@szu.edu.cn
†xiuwenzhang@szu.edu.cn

drift under electric operation. Furthermore, it is found that both V_{Cd} and Cd_i are shallow defects, suggesting a bipolar conduction with electron transport dominated due to the dispersive conduction-band minimum (CBM). We also find that the electron-rich Al_2CdS_4 structure can be both electrically conductive and optically transparent, which can be used to design potential transparent memristors. Our results could open the way of designing memristor materials among OVZ semiconductors with plenty of intrinsic vacancies for unique memristor properties as well as good compatibility with silicon and zincblende semiconductors.

II. COMPUTATIONAL METHODS

The first-principles calculations are performed based on density-functional theory (DFT) as implemented in the Vienna *Ab initio* Simulation Package (VASP) [37]. The electron-ion interactions are described by the projector augmented wave method [38], and we choose the Perdew–Burke–Ernzerhof functional within the generalized gradient approximation [39]. All the structures are fully relaxed, the energy cutoff of the ternary compound is set to 420 eV, and the forces acting on each atom are less than 0.01 eV $Å^{-1}$. In order to confirm the dynamical stability of the structure, the phonon spectra along the high-symmetry lines are calculated with the finite-displacement method as implemented in the PHONOPY package [40], where the precise convergence criterion for the total energy is 10^{-8} eV. In addition, the HSE06 [34] hybrid functional is also employed to confirm the band structures of the semiconducting phases. The climbing-image nudged elastic band method (CI-NEB) [35] is adopted to study the migration pathways of X atom in the supercell systems. The computational details of the optical property are presented in the Supplemental Material (SM) [41].

To calculate the defect properties of Al_2-X-Y_4, we construct a $4 \times 4 \times 2$ supercell that contains 512 atoms. Here, only the Γ point is used for all the calculations. For a defect α in the charge state q, its formation energy can be calculated by

$$\Delta H_f(\alpha, q) = \Delta E(\alpha, q) + \sum n_i \mu_i + q E_F, \qquad (1)$$

where $\Delta E(\alpha, q) = E(\alpha, q) - E(\text{host}) + \sum n_i E_i + q\varepsilon_{\text{VBM}}(\text{host})$. Here, $E(\text{host})$ is the total energy of the supercell and $E(\alpha, q)$ is the total energy of the same supercell, but with a defect α. The E_F is referenced to the valence-band maximum (VBM) of the host, μ_i is the chemical potential of constituent elements referenced to elemental solid with energy E_i, n_i is the number of elements, and q is the number of electrons transferred from the supercell to reservoirs in forming the defect cell. The transition-energy level of a defect α between charge states q and q', $\varepsilon_\alpha(q/q')$, with respect to the VBM, can be calculated from the formation energies by

$$\varepsilon_\alpha(q/q') = \frac{\Delta E(\alpha, q) - \Delta E(\alpha, q')}{q' - q} - \varepsilon_{\text{VBM}}. \qquad (2)$$

III. RESULTS AND DISCUSSION

A. Electronic structure and defect properties

We choose the Al_2-X-Y_4 (X = Zn, Cd; Y = S, Se, Te) group of compounds to demonstrate the modulable electric and optical properties of OVZ materials, since the Al-Y bonds in these compounds are strongly covalent for constructing a stable covalent framework. Figure 1(a) shows the crystal structure (space group No. 82) of Al_2CdS_4, with the vacancy sites illustrated by the red empty circles. It was reported that most of these Al_2-X-Y_4 OVZ structures have been synthesized experimentally [42,43], except for Al_2ZnS_4. However, the calculated phonon spectrum of Al_2ZnS_4 (see Fig. S1 in SM) confirms that this compound could be also dynamically stable, and its energy stability is only slightly higher (0.004 eV/atom) than the ground-state $Fd\bar{3}m$ phase. This evidence implies that the Al_2-X-Y_4 compounds may provide a realistic platform to study the modulable electric and optical properties of OVZ materials.

Figure 1(b) shows the calculated band structure of Al_2CdS_4 within the HSE06 method. The calculation reveals an indirect band gap of ~3.87 eV, indicating semiconducting (or insulating) property of Al_2CdS_4. The HSE06 band gaps of the other Al_2-X-Y_4 compounds are listed in Fig. 1(d), with the corresponding band structures given in Fig. S2. Notably, the calculated band gaps (3.87/2.96 eV) of Al_2CdS_4 and Al_2CdSe_4 are close to the corresponding experimental values (3.82/2.95 eV) from the absorption coefficient spectra [43], which indicates the reliability of the HSE06 calculations. It can be found that all the sulfides possess indirect band gaps, whereas the selenides and tellurides show direct band gaps. This should be ascribed to the fact that from sulfides to selenides and tellurides, the monotonic increase of their volume increases the size of the empty sites in the lattice, where the X-point conduction-band bottom resides. As a consequence, the energy of this X-point conduction-band bottom drops, which in turn pushes the X-point top valence-band down, resulting in the VBM shift from the X point in sulfides to the Γ point in selenides and tellurides (see Fig. S2). Moreover, it is interesting to see that the band gaps of Al_2-X-Y_4 compounds can be largely adjusted from 2.37 to 4.26 eV, by changing their compositions, suggesting variable potential applications of these materials. For example, the Al_2-X-S_4 and Al_2-X-Se_4 compounds all have relatively large band gaps (> 2.9 eV) and thus are transparent for most visible light, making them potential candidates as transparent conducting materials.

As potential memristor materials, it is highly required that the defect distributions of Al_2-X-Y_4 compounds can be easily modulated by electric field. To demonstrate this possibility, we first calculate the defect property of the typical Al_2CdS_4, as shown in Fig. 2. Al_2CdS_4 has experimental/calculated lattice constants of $a = 5.55$ Å/$a = 5.63$ Å, and $c = 10.11$ Å/$c = 10.24$ Å, and a small lattice mismatch (>0.35 and <2.5%) on Si/GaAs (001) substrates with experimental/calculated lattice constant of (Si: $a = 5.43$ Å/$a = 5.65$ Å, GaAs: $a = 5.47$ Å/$a = 5.75$ Å). From Eq. (1), it is clear to see that the defect formation energy (ΔH_f) relates closely to the chemical potential (μ_i), while μ_i is not a free variable, but restricted by a series of chemical conditions. First, to avoid the formation of elementary solids, it is required that $\mu_i < 0$. Second, to avoid the formation of secondary phases, such as CdS, μ_i must satisfy

$$\mu_{Cd} + \mu_S < \Delta H_f(\text{CdS}). \qquad (3)$$

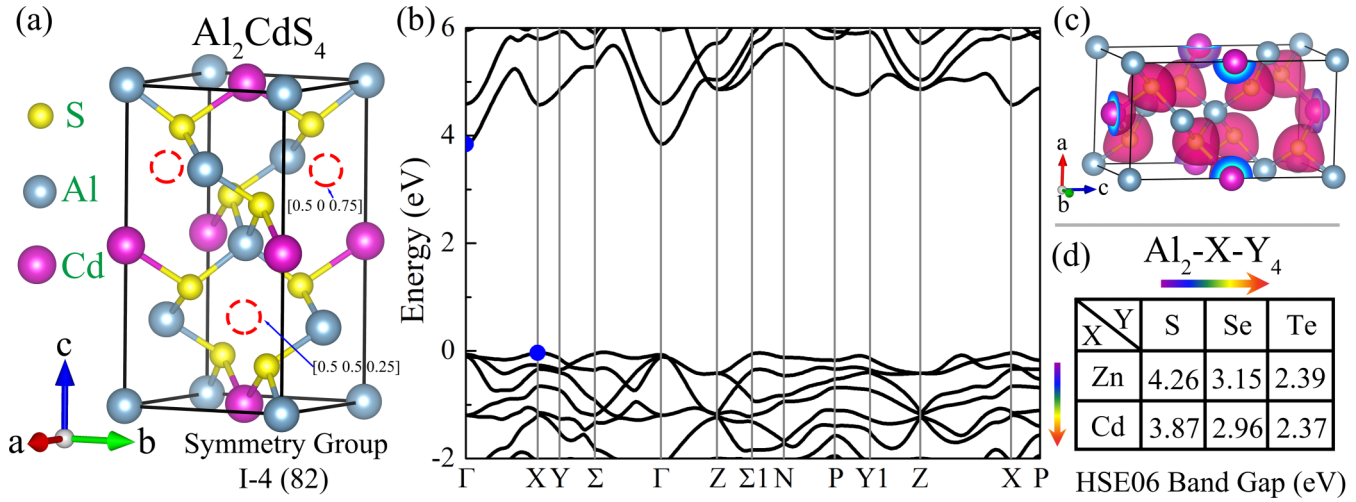

X \ Y	S	Se	Te
Zn	4.26	3.15	2.39
Cd	3.87	2.96	2.37

FIG. 1. (a) Crystal structure and symmetry group of Al_2CdS_4. (b) The HSE06 band structure of Al_2CdS_4, the blue dots represent the position of VBM and CBM. (The VBM is set to be 0.) (c) The calculated electron localization function of Al_2CdS_4. (d) The table presents the HSE06 band gaps of the Al_2-X-Y_4 (X = Zn, Cd; Y = S, Se, Te) compounds based on the structure of (a).

Similarly, other secondary phases should be also considered, such as CdS_2 (space group $Pa\bar{3}$) and Al_2S_3 (space group $P6_1$). Finally, to make Al_2CdS_4 stable, it is also required that

$$2\mu_{Al} + \mu_{Cd} + 4\mu_S = \Delta H_f(Al_2CdS_4). \quad (4)$$

With all these restrictions considered, the available chemical potential range is plotted in Fig. 2(a). At the point A (anion-rich condition), μ_{Al}, μ_{Cd}, and μ_S are calculated to be −3.02, −1.62, and 0.00 eV, respectively, while at the point B (cation-rich condition), μ_{Al}, μ_{Cd}, and μ_S are calculated to be −0.59, 0.00, and −1.62 eV, respectively.

Figure 2(b) shows the calculated formation energies of a series of possible defects in Al_2CdS_4 at both cation-rich and anion-rich conditions. At the cation-rich condition, the most favorable defects are positively changed Cd_i^{2+} and negatively changed V_{Cd}^{2-}, pinning the Fermi level (E_F) at 2.9 eV. The formation energy of both defects at the pinning point is about 0.5 eV, indicating the tunable feasibility of defect formation depending on growth temperature. Moreover, we find that some other defects, such as Al_{Cd}^{+}, Cd_{Al}^{-}, and Al_i^{3+} could also be probably created with a formation energy of 0.64, 0.64, and 0.78 eV at the pinning point, respectively. On the other hand, at the anion-rich condition, it is shown that the favorable defects are also Cd_i^{2+} and V_{Cd}^{2-} with the formation energy of 0.5 eV, pinning the E_F at 2.0 eV, while the formation energies of Al_{Cd}^{+}, Cd_{Al}^{-}, and Al_i^{3+} rise to be 0.58, 0.70, and 0.85 eV, respectively. From these calculations, one can see that the most possible defects in Al_2CdS_4 include three kinds of donors, Cd_i^{2+}, Al_{Cd}^{+}, and Al_i^{3+}, as well as two kinds of acceptors, V_{Cd}^{2-} and Cd_{Al}^{-}, which could be intentionally created by adjusting the synthesis environments. For the anion-rich condition, at the pinning point near the mid gap, all defects

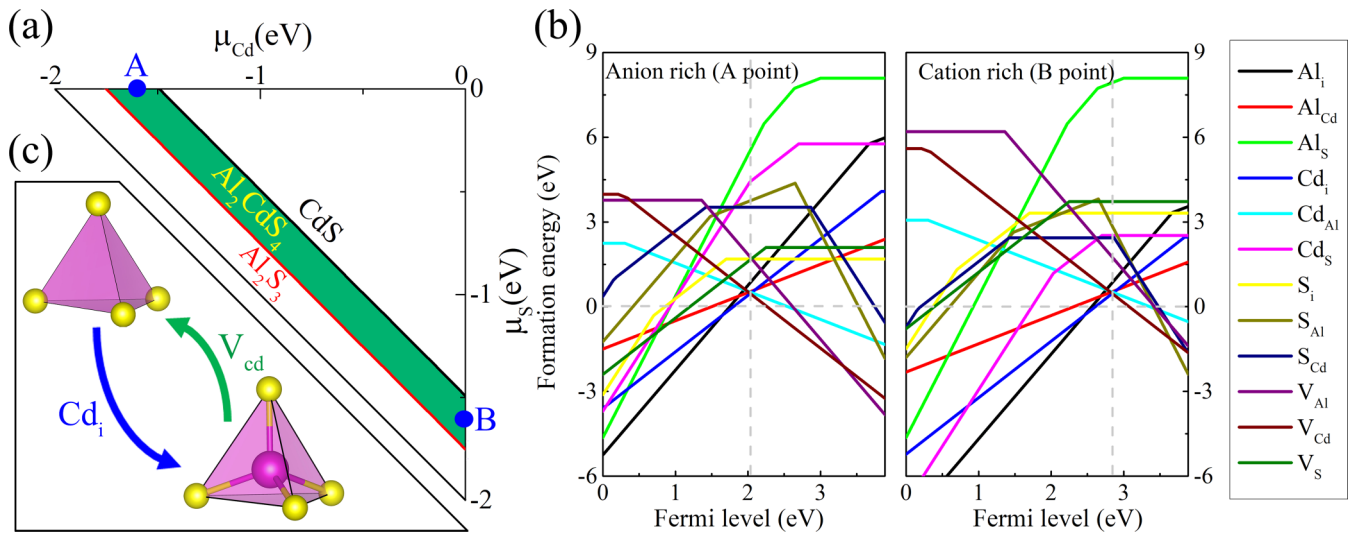

FIG. 2. (a) Stable chemical potential region for Al_2CdS_4; the potential competing phases are shown in the other regions. (b) Calculated formation energies for various defects in Al_2CdS_4, under both the Cd-rich and Cd-poor conditions. (c) Schematic diagram of the Cd_i/V_{cd} defects formation.

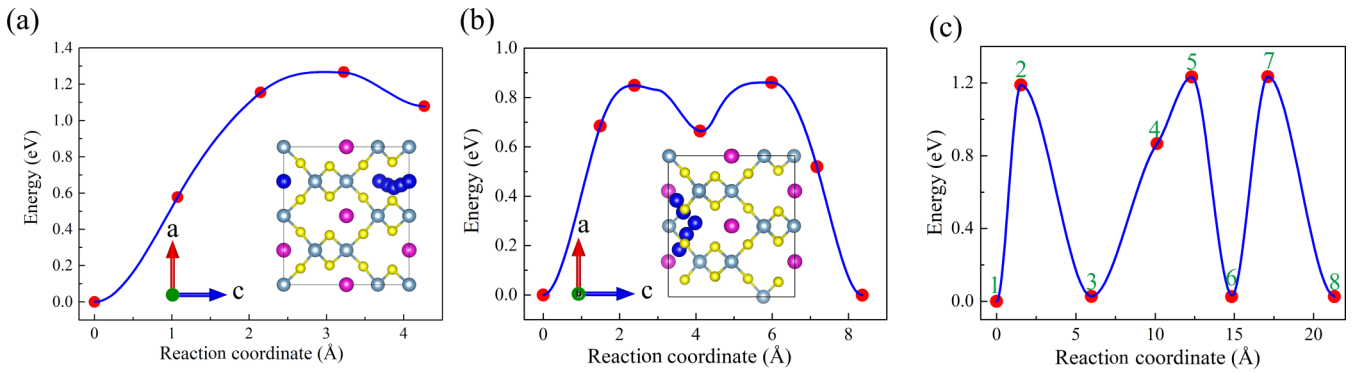

FIG. 3. (a) Representation of the minimum energy path of Cd atom diffusing to the Cd vacancy in the pristine (2 × 2 × 1) supercell of Al_2CdS_4 with a Cd vacancy. (b) Representation of the MEP of charged defect V_{Cd}^{2-} ion diffusing to the center of the adjacent S tetrahedron in the Cd-deficient (2 × 2 × 1) supercell of Al_2CdS_4. The blue dots in the insets describing the positions of the diffusing ions. (c) Representation of the MEP of the Cd_i^{2+} ion diffusing to the center of the adjacent S tetrahedron in the Cd-rich (2 × 2 × 1) supercell of Al_2CdS_4 (the corresponding CI-NEB images were presented in Fig. S4).

have formation energies above ∼0.5 eV, suggesting the possibility to realize high-resistance Al_2CdS_4 with rather low defect and carrier concentrations at low to medium synthesis temperature.

B. Diffusion path of the defects

For memristor materials, one would expect the drift movement of special defects under electric operation, such as the movement of oxygen vacancies in metal oxides [6,8]. In OVZ semiconductors, "cation vacancies" are already formed and distributed orderly in their original diamond structure. Thus, if one can drift these vacancies to accumulate at some region of the material (or equivalently drift the Cd ions from the region), while to deplete at another region (or equivalently to form Cd_i there), then OVZ semiconductors could demonstrate interesting memristor effect with transport of carriers and ions that are both abundant. For Al_2CdS_4, we expect this could be realized through manipulating the Cd ions by electric operation, i.e., to create Cd_i^{2+} at one side of the material and V_{Cd}^{2-} at another side, since both of these two defects have relatively low formation energies based on the defect calculations. As shown in Fig. 1(a) and Fig. 2(c), the S tetrahedra in Al_2CdS_4 not only provide a skeleton to accommodate Cd ions, but also perfect channels for Cd ion migration. However, one remaining critical question is whether these Cd ions are mobile in this anion-built skeleton, just like the oxygen vacancies in metal oxides. To answer this question, we next considered the diffusion property of Cd ions in Al_2CdS_4, as shown in Fig. 3. Although the vacancies/ions in memristors will undergo drift movement upon the electric operation, it is still relevant to evaluate the diffusion barrier of these vacancies/ions along the minimum energy path (MEP) in the absence of external voltage, because (i) the fast drift velocity is related to such diffusion barriers, and (ii) the slow back-diffusion of the accumulated species in the conductive filament is determined by the highest barrier along the MEP. Due to the special structural character of OVZ semiconductors, three different diffusion manners of Cd vacancies/ions in Al_2CdS_4 have been considered:

(i) The diffusion of a Cd ion from its original position in pristine crystal to the nearby vacancy site, i.e., the diffusion of a vacancy from its original position to form a Cd_i-V_{Cd} defect pair that could be driven by the electric operation, which could represent the initial generation of electrically active defects for separating the ion- and vacancy-rich regions. We simulate this case by removing one Cd atom in a 2 × 2 × 1 supercell of the pristine Al_2CdS_4 to create a V_{Cd} and study the diffusion of this V_{Cd}, i.e., the jumping of this V_{Cd} into adjacent Cd sites, as shown in Fig. 3(a). It can be seen that the MEP of V_{Cd} has a zigzag shape with an energy barrier of 1.26 eV.

(ii) The diffusion of a cation vacancy defect, V_{Cd}, in the Cd-deficient region. The results for charged defect V_{Cd}^{2-} are given in Fig. 3(b), showing a conjugated diffusion path of Cd ions/vacancies with an energy barrier of 0.86 eV. The results for neutral defect V_{Cd} are given in Fig. S3(a). According to the defect calculations in Fig. 2(b), V_{Cd} defect will be ionized for most of the E_F inside the band gap.

(iii) The diffusion of Cd ion in the Cd-rich region. We simulate this case by creating a cation interstitial defect, Cd_i, in the pristine Al_2CdS_4 structure and study its diffusion into adjacent virtual vacancy sites. The results for charge-neutral cation interstitial Cd_i are shown in Fig. S3(b), giving a linear diffusion path with a relatively high energy barrier of 2.3 eV. According to the defect calculations in Fig. 2(b), the Cd_i is easy to be ionized, and the physical truth should be the diffusion of Cd_i^{2+} ion. As shown in Fig. 3(c), the Cd_i^{2+} ion will pass the internal S-Cd net by Cd ion comovement (see Fig. S4), and the MEP barrier of this complicated path is only 1.23 eV.

It is worth to note that the energy barriers for the above diffusion of Cd vacancies/ions in Al_2CdS_4 are quite similar to the diffusion barriers of vacancies/ions in metal-oxide memristor materials [4,36]. Compared with the oxide memristor materials like ZnO and TiO_2 [36,44], the Cd atom diffusing barrier in Al_2CdS_4 is moderate (see Table S2). Analogous to metal-oxide memristor materials, the diffusion barriers of Cd vacancies/ions in Al_2CdS_4 should be suitable for their drift movement under electric operation, while, in back-diffusion process, the actual defective vacancy (as opposed to the

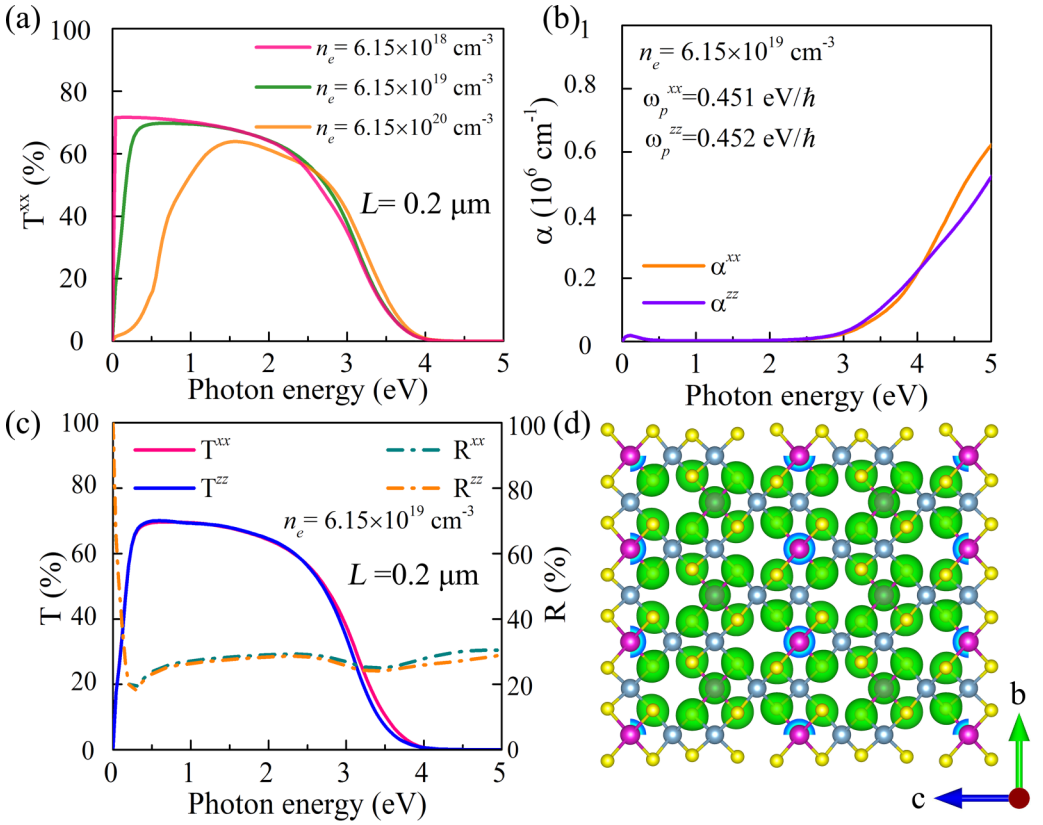

FIG. 4. (a) The transmission spectra (T_{xx}) of a freestanding 0.2-μm-thick Al_2CdS_4 slab with various carrier densities (n_e). (b) The absorption coefficient ($\alpha^{xx} = \alpha^{yy}$, α^{zz}) of Al_2CdS_4 with $n_e = 6.15 \times 10^{19}$ cm^{-3}, and plasma frequency ($\omega_p^{xx} = \omega_p^{yy} = 0.451$ eV/$\hbar$, $\omega_p^{zz} = 0.452$ eV/$\hbar$) are given in the inset of (b). (c) The transmission spectra ($T_{xx} = T_{yy}$, T_{zz}) of a freestanding 0.2-μm-thick Al_2CdS_4 slab with optically smooth surfaces ($n_e = 6.15 \times 10^{19}$ cm^{-3}). (d) Representation of the real-space electron density distribution (green spheres) of the above doped system. The electrical conductivity evaluated from the plasma frequency is σ^{xx}=$\sigma^{yy} = 0.136 \times 10^3$ S/cm; $\sigma^{zz} = 0.136 \times 10^3$ S/cm. Note that, the blue spheres represent the internal sections of the green spheres. See Supplemental Material Sec. I for the evaluation methods for optical property and conductivity.

virtual vacancy in the pristine Al_2CdS_4) needs to diffuse to the position of actual defective Cd interstitial to be annihilated, or equivalently the latter needs to diffuse to the former. Thus, for back-diffusion that determines the lasting time of the conductive filament, any of the high barriers along the MEP can hinder the diffusion. Therefore, under external voltage of the electric operation, the vacancy-rich region versus ion-rich region in Al_2CdS_4 compounds could be generated, forming conductive filaments. From Fig. 2(b), we see that both Cd_i and V_{Cd} are shallow defects, with the corresponding transition-energy levels lying above the CBM and 0.2 eV above the VBM, respectively. Thus, both the vacancy-rich and ion-rich regions are potential conductive filaments, suggesting a possible bipolar conduction process in OVZ memristor materials. For other Al_2-X-Y_4 compounds, similar defect and diffusion properties could be expected, due to the analogous physical and chemical properties of the constitute elements in the same column in the periodic table. In theory, various similar principles to design memristor devices have been widely explored for the metal oxide. For example, within the ideal lattice mismatch, the interdiffusion of Ag atoms into the oxide phase or of O atoms into the metal electrode at the TiO_2/Ag interfaces can be modeled for memristor designing [45]. In addition, understanding the microscopic behavior of the oxygen vacancies in metal oxide by theoretical calculation is crucial to verify the defects controlling the resistance switching mechanism in practical memristor materials [44].

C. Optical properties of the doped Al_2CdS_4

As Al_2CdS_4 has a wide band gap of 3.87 eV, it is worthwhile to consider Al_2CdS_4 as a potential transparent memristor material. We use the pristine Al_2CdS_4 structure with doping 0.001/0.01/0.1 electron per primitive cell to mimic the dilute limit of Cd doping in Al_2CdS_4. Clearly, the three magnitudes of electron carrier density (n_e) lead to the closely high transmittance for most visible light [see Fig. 4(a)]. Thus, we adopted the moderate carrier density ($n_e = 6.15 \times 10^{19}$ cm^{-3}) to study the corresponding optical properties of the n-type Al_2CdS_4. We found that the electric conductivity ($\sigma^{xx} = \sigma^{yy} = 0.136 \times 10^3$ S/cm, $\sigma^{zz} = 0.136 \times 10^3$ S/cm), as estimated from the plasma frequency [$\omega_p^{xx} = \omega_p^{yy} = 0.451$ eV/$\hbar$, $\omega_p^{zz} = 0.452$ eV/$\hbar$ shown in Fig. 4(b)] of the dilute electron-doped structure with doping level of 6.15×10^{19} cm^{-3} is already quite high, suggesting the material as a good electric conductor. On the other hand, the calculated optical absorption coefficients with the consideration of plasma effects indicate that this dilute electron-doped structure has rather

low optical absorption for visible light, as shown in Fig. 4(b). The optical simulation for a 0.2-μm-thick slab of the doped structure predicts rather a high optical transmittance as can be seen from Fig. 4(c). Figure 4(d) shows the real-space electron density of the above doped system, indicating uniform distribution of carriers. The combination of high electric conductivity and high optical transparency found in Cd-rich Al_2CdS_4 may suggest the potential use of this material as transparent memristors.

In the actual case, the defect formation is driven by the external electric field and the defect concentration in this nonequilibrium condition would be much higher than the equilibrium case. By carefully controlling the applied electric field, the defect concentration and thus the charge concentration can be well controlled. Thus, we considered a moderate charge concentration $n_e = 6.15 \times 10^{19}\,\mathrm{cm}^{-3}$, which already gives a quite high electronic conductivity. For the convenience of discussion, the lower and higher n_e calculated results are presented in Fig. S5, which indicates the adjustable transparent conductive properties of Al_2CdS_4. The transparent conductive Al_2CdS_4 could be used in transparent memristors constructed by using Al_2CdS_4 as memristor material and doped ZnS [46,47] as transparent electrodes (see, e.g., Fig. S6). The lattice mismatch between ZnS (zincblende) and Al_2CdS_4 (OVZ) can be as small as 3% for their (001) interface of the zincblende-like lattice, according to our DFT calculations.

The plasma frequencies (electric conductivities) of other Al_2-X-Y_4 semiconductors are given in Table S1, and the corresponding absorption coefficient and transmission spectra are shown in Figs. S7 and S8. It should be noted that the used damping coefficient ($\gamma = 0.2\,\mathrm{eV}/\hbar$) analogous to In_2O_3 [48] could be too large for the diamondlike Al_2-X-Y_4 semiconductors, and thus the above-estimated electric conductivities from $\frac{(\omega_p^{ij})^2}{4\pi\gamma}$ could be underestimated.

IV. CONCLUSIONS

In summary, we have studied the electric and optical properties of the Al_2-X-Y_4 group of OVZ semiconductors, and select Al_2CdS_4 as the best candidate that is lattice-matched to Si, showing medium energy barriers of $\sim$1 eV for vacancy/ion diffusion, comparable to the metal-oxide memristor materials. We find from defect calculations that both V_{Cd} and Cd_i are shallow defects, giving a bipolar conduction in the candidate memristor Al_2CdS_4. We further find that the electron-rich Al_2CdS_4 structure can be both electrically conductive and optically transparent, with potential applications in transparent memristors. These highly defective diamondlike ordered-vacancy semiconductors could be a complementary materials system of defect-free diamondlike semiconductors in electronic technologies. As for memristor applications, the OVZ semiconductors could have a few optimum properties: (i) better compatibility with other diamondlike semiconductors used in electronic technologies; (ii) diversity of band gap and optical properties covering infrared to visible optical spectrum for designing materials in electronic as well as optoelectronic memristor devices; (iii) the vacancies in the pristine OVZ compounds are virtual and not electrically active leading to very high OFF-state resistivity as compared to the memristor materials based on defective vacancies; (iv) the virtual defects in OVZ materials are very abundant, offering the possibility of forming wide conductive filaments for lower ON-state resistivity; (v) the equilibrium state of the OVZ system with uniform vacancy distribution is a ground state in the phase diagram leading to the possibility of fully recovery from the accumulation of defects in the formation of conductive filaments to the equilibrium ground state after a medium long time, thus sustaining for long-term reusage; (vi) the abundant vacancies and the associated cations in the pristine OVZ material could speed up the formation and destruction process of the conductive filaments, leading to high operation frequencies of the memristors. Our study opens the way of designing virtual-defect abundant semiconductors for electronic applications that involve both electronic and ionic transport.

ACKNOWLEDGMENTS

This work is supported by Shenzhen Science and Technology Innovation Commission (Grants No. JCYJ20170818093035338, No. KQTD20180412181422399, and No. KQTD20170810105439418), National Natural Science Foundation of China (Grants No. 11774239 and No. 61827815), National Key R&D Program of China (Grant No. 2016YFB0700700), Postdoctoral Science Foundation of China (Grant No. 2019M652996), and High-Level University Construction Funds of SZU (Grant No. 860–000002081209).

[1] L. O. Chua, IEEE Trans. Circuit Theory **18**, 507 (1971).
[2] D. B. Strukov, G. S. Snider, D. R. Stewart, and R. S. Williams, Nature (London) **453**, 80 (2008).
[3] M. Laurenti, S. Porro, C. F. Pirri, C. Ricciardi, and A. Chiolerio, Crit. Rev. Solid State Mater. Sci. **42**, 153 (2017).
[4] U.-B. Han, D. Lee, and J.-S. Lee, NPG Asia Mater. **9**, e351 (2017).
[5] C.-H. Huang, J.-S. Huang, C.-C. Lai, H.-W. Huang, S.-J. Lin, and Y.-L. Chueh, ACS Appl. Mater. Inter. **5**, 6017 (2013).
[6] Z. Q. Wang, H. Y. Xu, X. H. Li, H. Yu, Y. C. Liu, and X. J. Zhu, Adv. Funct. Mater. **22**, 2759 (2012).
[7] H. Tan, G. Liu, H. Yang, X. Yi, L. Pan, J. Shang, S. Long, M. Liu, Y. Wu, and R.-W. Li, ACS Nano **11**, 11298 (2017).
[8] J. Yin, F. Zeng, Q. Wan, F. Li, Y. Sun, Y. Hu, J. Liu, G. Li, and F. Pan, Adv. Funct. Mater. **28**, 1706927 (2018).
[9] F. Miao, J. P. Strachan, J. J. Yang, M.-X. Zhang, I. Goldfarb, A. C. Torrezan, P. Eschbach, R. D. Kelley, G. Medeiros-Ribeiro, and R. S. Williams, Adv. Mater. **23**, 5633 (2011).
[10] W. Huang, Y.-W. Fang, Y. Yin, B. Tian, W. Zhao, C. Hou, C. Ma, Q. Li, E. Y. Tsymbal, C.-G. Duan, and X. Li, ACS Appl. Mater. Inter. **10**, 5649 (2018).

[11] R. Guo, Y. Zhou, L. Wu, Z. Wang, Z. Lim, X. Yan, W. Lin, H. Wang, H. Y. Yoong, S. Chen, Ariando, T. Venkatesan, J. Wang, G. M. Chow, A. Gruverman, X. Miao, Y. Zhu, and J. Chen, ACS Appl. Mater. Inter. **10**, 12862 (2018).

[12] T.-H. Lee, H.-G. Hwang, J.-U. Woo, D.-H. Kim, T.-W. Kim, and S. Nahm, ACS Appl. Mater. Inter. **10**, 25673 (2018).

[13] Y. Li, J. Chu, W. Duan, G. Cai, X. Fan, X. Wang, G. Wang, and Y. Pei, ACS Appl. Mater. Inter. **10**, 24598 (2018).

[14] X. Yan, J. Zhao, S. Liu, Z. Zhou, Q. Liu, J. Chen, and X. Y. Liu, Adv. Funct. Mater. **28**, 1705320 (2018).

[15] K. Qian, G. Cai, N. Viet Cuong, T. Chen, and P. S. Lee, ACS Appl. Mater. Inter. **8**, 27885 (2016).

[16] B. R. Pamplin, Nature (London) **188**, 136 (1960).

[17] G. L. W. Hart and A. Zunger, Phys. Rev. Lett. **87**, 275508 (2001).

[18] A. Walsh and A. Zunger, Nat. Mater. **16**, 964 (2017).

[19] W. Zhang, A. Thiess, P. Zalden, R. Zeller, P. H. Dederichs, J. Y. Raty, M. Wuttig, S. Bluegel, and R. Mazzarello, Nat. Mater. **11**, 952 (2012).

[20] G. M. Dalpian, Q. Liu, C. C. Stoumpos, A. P. Douvalis, M. Balasubramanian, M. G. Kanatzidis, and A. Zunger, Phys. Rev. Mater. **1**, 025401 (2017).

[21] M.-G. Ju, M. Chen, Y. Zhou, H. F. Garces, J. Dai, L. Ma, N. P. Padture, and X. C. Zeng, ACS Energy Lett. **3**, 297 (2018).

[22] A. E. Maughan, A. M. Ganose, A. M. Candia, J. T. Granger, D. O. Scanlon, and J. R. Neilson, Chem. Mater. **30**, 472 (2018).

[23] A. Jannat, Q. Yao, A. Zavabeti, N. Syed, B. Y. Zhang, T. Ahmed, S. Kuriakose, M. Mohiuddin, N. Pillai, F. Haque, G. Ren, D. M. Zhu, N. Cheng, Y. Du, S. A. Tawfik, M. J. S. Spencer, B. J. Murdoch, L. Wang, C. F. McConville, S. Walia, T. Daeneke, L. Zhu, and J. Z. Ou, Mater. Horiz. **7**, 827 (2020).

[24] K.-Y. Yeh, T.-S. Lo, P. M. Wu, K.-S. Chang-Liao, M.-J. Wang, and M.-K. Wu, Proc. Natl. Acad. Sci. U. S. A **117**, 12606 (2020).

[25] S. M. Sze and K. K. Ng, *Physics of Semiconductor Devices*, 3rd ed. (John Wiley & Sons, Hoboken, NJ, 2006) .

[26] T. Okamoto, N. Kojima, and A. Yamada, Jpn. J. Appl. Phys. **31**, L143 (1992).

[27] J. E. Bernard and A. Zunger, Phys. Rev. B **37**, 6835 (1988).

[28] X. S. Jiang and W. R. L. Lambrecht, Phys. Rev. B **69**, 035201 (2004).

[29] S. B. Zhang, S. H. Wei, and A. Zunger, Phys. Rev. Lett. **78**, 4059 (1997).

[30] C. H. Chang, S. H. Wei, J. W. Johnson, S. B. Zhang, N. Leyarovska, G. Bunker, and T. J. Anderson, Phys. Rev. B **68**, 054108 (2003).

[31] C. Rincon, S. M. Wasim, G. Marin, J. M. Delgado, J. R. Huntzinger, A. Zwick, and J. Galibert, Appl. Phys. Lett. **73**, 441 (1998).

[32] G. Marin, J. M. Delgado, S. M. Wasim, C. Rincon, G. S. Perez, A. E. Mora, P. Bocaranda, and J. A. Henao, J. Appl. Phys. **87**, 7814 (2000).

[33] H. Abunahla and B. Mohammad, *Memristor Technology: Synthesis and Modeling for Sensing and Security Applications* (Springer, New York, 2018).

[34] J. Heyd, G. E. Scuseria, and M. Ernzerhof, J. Chem. Phys. **118**, 8207 (2003).

[35] G. Henkelman, B. P. Uberuaga, and H. Jónsson, J. Chem. Phys. **113**, 9901 (2000).

[36] P. Erhart and K. Albe, Phys. Rev. B **73**, 115207 (2006).

[37] G. Kresse and J. Furthmüller, Phys. Rev. B **54**, 11169 (1996).

[38] G. Kresse and D. Joubert, Phys. Rev. B **59**, 1758 (1999).

[39] J. P. Perdew, K. Burke, and M. Ernzerhof, Phys. Rev. Lett. **77**, 3865 (1996).

[40] A. Togo, F. Oba, and I. Tanaka, Phys. Rev. B **78**, 134106 (2008).

[41] See Supplemental Material at http://link.aps.org/supplemental/10.1103/PhysRevMaterials.5.024603 for the details of electrical conductivity, the HSE06 band structures, and the absorption and transmission spectra for the Al_2-X-Y_4 compounds.

[42] H. Hahn, G. Frank, W. Klingler, A. D. Störger, and G. Störger, Z. Anorg. Allg. Chem. **279**, 241 (1955).

[43] G. Krauss, V. Kramer, A. Eifler, V. Riede, and S. Wenger, Cryst. Res. Technol. **32**, 223 (1997).

[44] A. Paris and S. Taioli, J. Phys. Chem. C **120**, 22045 (2016).

[45] S. Prada, M. Rosa, L. Giordano, C. Di Valentin, and G. Pacchioni, Phys. Rev. B **83**, 245314 (2011).

[46] P. D'Amico, A. Calzolari, A. Ruini, and A. Catellani, Sci. Rep. **7**, 16805 (2017).

[47] S. K. Maurya, Y. Liu, X. Xu, R. Woods-Robinson, C. Das, J. W. Ager III, and K. R. Balasubramaniam, J. Phys. D: Appl. Phys. **50**, 505107 (2017).

[48] G. V. Naik, J. Kim, and A. Boltasseva, Opt. Mater. Express **1**, 1090 (2011).